Superconducting properties in doped 2M-WS_2 from first principles

Journal:	*Journal of Materials Chemistry C*
Manuscript ID	TC-ART-03-2022-001173.R1
Article Type:	Paper
Date Submitted by the Author:	23-Apr-2022
Complete List of Authors:	Paudyal, Hari; SUNY Binghamton, Department of Physics, Applied Physics, and Astronomy Margine, E. R.; SUNY Binghamton, Department of Physics, Applied Physics, and Astronomy

Superconducting properties in doped 2M-WS$_2$ from first principles

Hari Paudyal[1] and Elena R. Margine[1,*]

[1] *Department of Physics, Applied Physics, and Astronomy,*
Binghamton University-SUNY, Binghamton, New York 13902, USA

(Dated: April 23, 2022)

A new member of the transition metal dichalcogenide (TMD) family, 2M-WS$_2$, has been recently discovered and shown to display superconductivity with a critical temperature (T_c) of 8.8 K, the highest T_c among superconducting TMDs at ambient pressure. Using first-principles calculations combined with the Migdal-Eliashberg formalism, we explore how the superconducting properties of 2M-WS$_2$ can be enhanced through doping. Mo, Nb, and Ta are used as dopants at the W sites, while Se at the S sites. We demonstrate that the monotonous decrease in the T_c observed experimentally for Mo and Se doping is due to the decrease in density of states at the Fermi level and the electron-phonon coupling of the low-energy phonons. In addition, we find that a noticeable increase in the electron-phonon coupling could be achieved when doping with Nb and Ta, leading to an enhancement of the T_c up to 50% compared to the undoped compound.

INTRODUCTION

Transition metal dichalcogenides (TMDs) are among the most studied van der Waals layered materials with unique physical and chemical properties that have found a broad range of applications in electronics, optoelectronics and energy storage [1–3]. TMDs can adopt hexagonal (2H), trigonal (1T), orthorhombic (T$_d$), or monoclinic (1T$'$) crystal structures, with different stacking sequences of individual MX$_2$ layers (M = transition metal, X = chalcogen) [4, 5]. As a result, this class of materials exhibits a wide variety of electronic properties, ranging from insulating to metallic. For example, 1T-HfS$_2$ is an insulator with a band gap of $\sim$2 eV [6, 7], 2H-MoS$_2$ and 2H-WS$_2$ are semiconductors with high mobility [8, 9] and promising materials for valleytronics [10, 11], T$_d$-WTe$_2$ and T$_d$-MoTe$_2$ are Weyl semimetals with large magnetoresistance and pressure-driven superconductivity [4, 12, 13], and 2H-NbS$_2$ and 2H-NbSe$_2$ are metals with superconducting and charge density wave transitions [14–17].

Recently, in group VI-TMDs, two new members 2M-WS$_2$ and 2M-WSe$_2$ have been synthesized by deintercalation of potassium ions from K$_x$WS$_2$ and K$_x$WSe$_2$ crystals, respectively [5, 18]. The resulting compounds are both metallic, and 2M-WS$_2$ exhibits superconductivity with a critical temperature (T_c) of 8.8 K, the highest T_c among superconducting TMDs at ambient pressure. In addition to being superconducting, this phase has been predicted [5, 19], and later confirmed [20], to display topologically protected surface states with a single Dirac cone at the Brillouin zone (BZ) center. On the other hand, in the sister compound 2M-WSe$_2$, superconductivity only appears under pressure at 4.2 GPa, and the critical temperature reaches a maximum value of 7.3 K at 10.7 GPa [21].

The superconductivity in 2M-WS$_2$ has been further examined in muon spin relaxation/rotation [22], low temperature thermal conductivity [23], and scanning tunneling microscopy [24] experiments. These studies have suggested either a single gap with s-wave symmetry [22] or anisotropic multiple superconducting gaps [23, 24], respectively. A recent theoretical study using the Migdal-Eliashberg (ME) formalism [25, 26] has shown that both bulk and bilayer 2M-WS$_2$ are single anisotropic full gap s-wave superconductors [27]. Finally, few experiments have been carried out to understand the effect of pressure and doping (with Mo and Se) on the superconducting properties of 2M-WS$_2$, and found that both have a negative effect on the T_c [22, 28, 29]. These findings motivated us to examine the superconductivity in 2M-WS$_2$ more closely and explore if the critical temperature can be further enhanced through doping.

In the present work, we applied the ME theory [26, 30] to investigate the superconducting properties of 2M-W$_{1-x}$X$_x$S$_2$ (X = Mo, Nb and Ta) and 2M-WS$_{2(1-x)}$Se$_{2x}$. Doping was simulated using chemical substitution at the W and S sites or employing the virtual crystal approximation (VCA) method. We found that 2M-W$_{1-x}$Mo$_x$S$_2$ and 2M-WS$_{2(1-x)}$Se$_{2x}$ are dynamically stable within the full doping range $0 \leq x \leq 1$, while 2M-W$_{1-x}$Na$_x$S$_2$ and 2M-W$_{1-x}$Ta$_x$S$_2$ for $0 \leq x \leq 0.5$. We showed that the drop in the T_c observed experimentally for Mo and Se doping [28, 29] is due to the decrease in the density of states at the Fermi level (N_F) and the electron-phonon (e-ph) coupling of the low-frequency phonons. Furthermore, we predict that the e-ph coupling, and subsequently the critical temperature, can be enhanced if doping levels up to 50% can be achieved for Nb or Ta.

METHODS

The *ab initio* calculations were carried out with the Quantum ESPRESSO (QE) [31] package. We used relativistic optimized norm-conserving Vanderbilt pseudopotentials [32, 33] with the Perdew-Burke-Ernzerhof (PBE) [34] exchange-correlation functional in the gen-

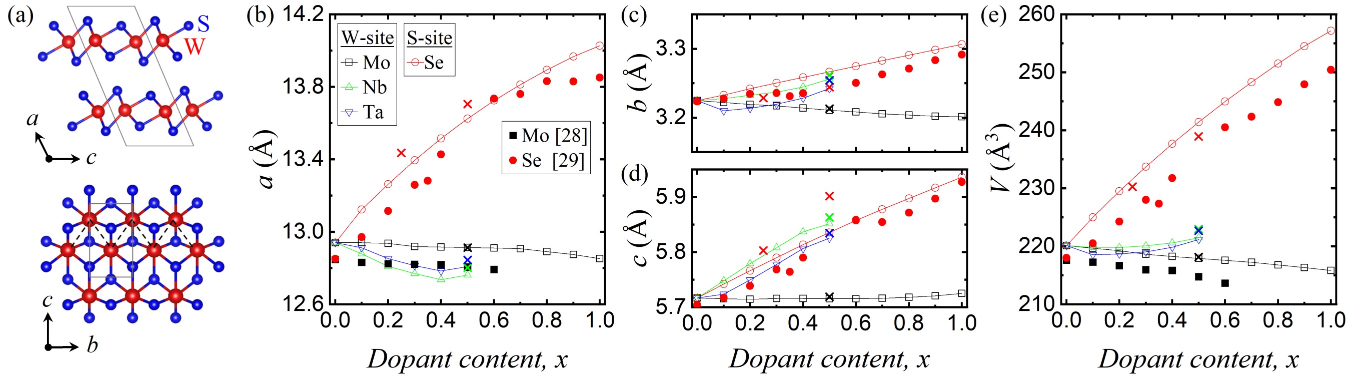

FIG. 1. (a) Crystal structures of 2M-WS_2. (b-d) Variation of lattice parameters and volume of 2M-WS_2 as a function of doping content x. Computational results with substitutional doping and the VCA method are shown with cross and open symbols. Experimental data for Mo [28] and Se [29] doping are shown with filled symbols.

eralized gradient approximation. To properly treat the long-range dispersive interactions, we employed the non-local van der Waals density functional optB86b-vdW [35–37]. A plane wave kinetic-energy cutoff value of 60 Ry, a Γ-centered $12\times12\times12$ Monkhorst-Pack **k**-mesh [38], and a Methfessel and Paxton smearing [39] width of 0.01 Ry were used for the BZ integration. The atomic positions and lattice parameters were optimized until the self-consistent energy was converged within 2.7×10^{-5} eV and the maximum Hellmann-Feynman force on each atom was less than 0.005 eV/Å. For the density of states, we used a denser $30\times30\times30$ **k**-mesh and a lower smearing value of 7.35×10^{-5} Ry. Chemical substitution of W and S was used to simulate doping at $x = 0.5$ (i.e., 50%) with Mo, Na, and Ta, and $x = 0.25$ (25%) and $x = 0.5$ (50%) with Se, respectively. To investigate intermediate compositions that would had required large supercells with substitutional doping, we used instead the VCA method. The structural analysis was performed with the MAISE package [40]. The dynamical matrices and the linear variation of the self-consistent potential were calculated within density-functional perturbation theory [41] on the irreducible set of a regular $4\times4\times4$ **q**-mesh.

The isotropic ME formalism implemented in the EPW code [25, 26, 30, 42] was used to investigate the superconducting properties. The Wannier interpolation [43, 44] was performed on a uniform Γ-centered $8\times8\times8$ grid with 22 maximally localized Wannier functions (five d-orbitals for each W atom and three p-orbitals for each S atom). The isotropic Eliashberg spectral function was computed for uniform $30\times30\times30$ **k**- and **q**-point grids, with Gaussian smearing values of 25 meV for electrons and 0.1 meV for phonons. The Matsubara frequency cutoff was set to 0.5 eV and the Coulomb pseudopotential to 0.1 when solving the isotropic ME equations.

CRYSTAL STRUCTURE

2M-WS_2 crystallizes in the monoclinic crystal structure with inversion symmetry (space group $C2/m$, No. 12). The unit cell consists of individual 1T′ monolayers as in 1T′-WTe_2 and T_d-$MoTe_2$ but displays a different stacking order along the direction perpendicular to the atomic layers. Note that the unit cell axes parallel to the atomic layers are chosen as b and c, while the axis oriented perpendicular to the layers as a. As shown in Fig. 1(a), the position of the W atoms is away from the octahedral center leading to a zigzag pattern along the b direction. The primitive unit cell consists of six atoms, where the two W atoms occupy one interdependent Wyckoff site 4i (0.743817; 0.5; 0.796634), and the four S atoms occupy two independent Wyckoff sites 4i (0.859592; 0.0; 0.678023) and 4i (0.604765; 0.0; 0.787555). The optimized lattice parameters a = 12.941 Å, b = 3.225 Å, c = 5.717 Å, and β = 112.691° are consistent with previous experimental and theoretical results [5, 24].

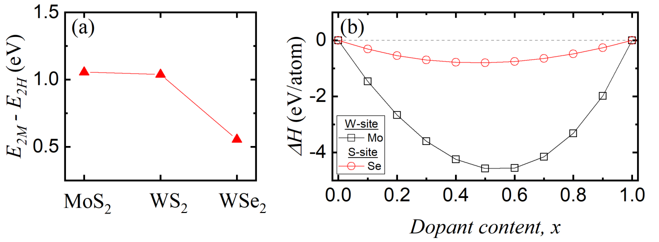

FIG. 2. (a) Energy difference between the 2M and 2H phases of group VI TMDs. (b) Formation enthalpy as a function of dopant content x.

Figure 1(b-d) shows the dependence of the lattice parameters as a function of the doping concentration. As the S content is reduced by doping with Se, the unit cell volume increases very rapidly since longer covalent

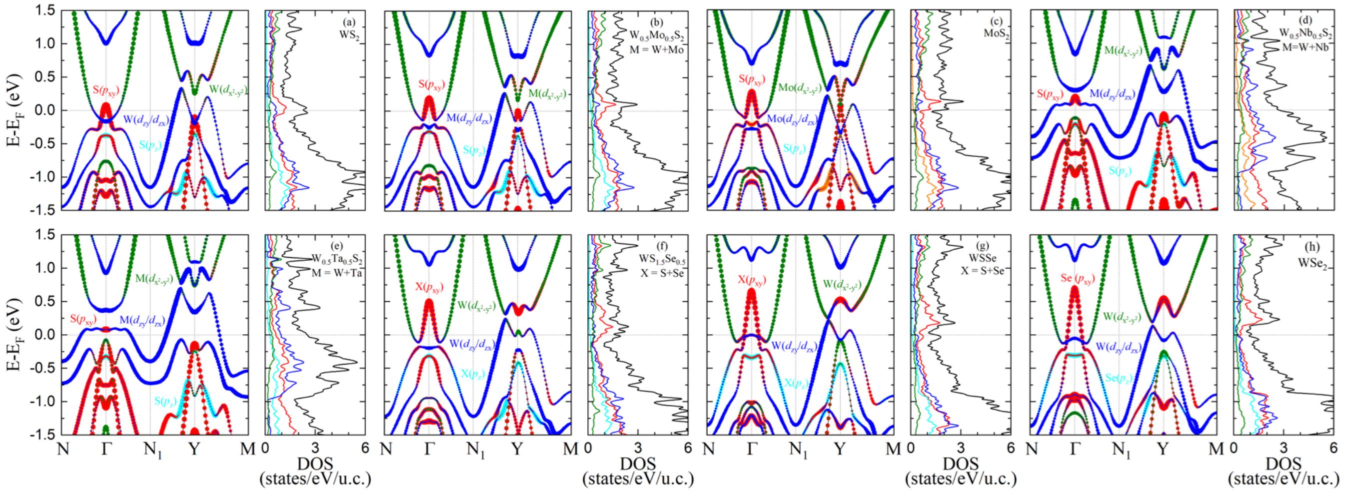

FIG. 3. Electronic band structure and DOS of (a) WS$_2$, (b) W$_{0.5}$Mo$_{0.5}$S$_2$, (c) MoS$_2$, (d) W$_{0.5}$Nb$_{0.5}$S$_2$, (e) W$_{0.5}$Ta$_{0.5}$S$_2$, (f) WS$_1$.5Se$_0$.5, (g) WSSe, and (h) WSe$_2$ in the 2M phase. The orbital characters are shown on the band structure with the size of the colored dots proportional to the weight of the orbital contribution.

intra-layer bonds are formed for the larger size dopant atom [45]. As expected, only a small variation is found when replacing W with Mo since the ionic radius of Mo is only slightly smaller than that of W. For instance, the in-plane parameters b and c remain at an almost constant value. Our results compare well with the experimental data extracted for polycrystalline samples doped with Mo and Se [28, 29]. In both cases, the lattice parameters and volume display a nearly linear dependence with doping according to Vegards law, which indicates that no phase transition takes place for isovalent doping and the dopants simply substitute the atoms of the parent 2M-WS$_2$ compound.

Next we investigate what happens when doping at the W sites with the slightest larger Nb and Ta atoms. Being placed at the left of W in the periodic table, these elements have one less d-electron, making the system p-doped. In this case, the out-of-plane and in-plane lattice parameters change in opposite directions; a contracts, while b and c expand, the net result being a small variation of the unit cell volume. Another important finding is that for both Nb and Ta doping, the system becomes dynamically unstable above $x > 0.5$, and undergoes a phase transition from the monoclinic 2M to the trigonal 1T crystal structure (space group $P\bar{3}m_1$, No. 164).

To gain insight into the energetic stability of the 2M phases at ambient pressure we computed the energy difference between the 2M and 2H phases of MoS$_2$, WS$_2$, and WSe$_2$ compounds. As shown in Fig. 2(a), the 2H crystal structure is found to be the ground state in all cases. Despite being approximately 0.56 eV and 1.04 eV higher in energy compared to the 2H phase, 2M-WSe$_2$ and 2M-WS$_2$ have been synthesized via deintercalation of interlayer potassium cations from K$_x$WSe$_2$ and K$_{0.7}$WS$_2$ crystals, respectively [5, 18]. Based on these results, it is highly possible that the 2M metastable phase of MoS$_2$ can also be synthesized using similar experimental techniques. We also checked the stability of the W$_{1-x}$Mo$_x$S$_2$ and 2M-WS$_{2(1-x)}$Se$_{2x}$ alloys with respect to their parent compounds. For example, the formation enthalpy ΔH of W$_{1-x}$Mo$_x$S$_2$ is defined as: $\Delta H(x) = (1-x)E(WS_2)+xE(MoS_2)-E(W_{1-x}Mo_xS_2)$, where E represents the energy of each compound and x is the dopant content. As illustrated in Fig. 2(b), we find that the $T = 0$ K formation enthalpy is negative across the entire composition range, which suggests that both W$_{1-x}$Mo$_x$S$_2$ and 2M-WS$_{2(1-x)}$Se$_{2x}$ alloys are stable with respect to decomposition into the parent compounds.

ELECTRONIC PROPERTIES

Figure 3(a) shows the electronic band structure of 2M-WS$_2$ with atomic orbital decomposition. A characteristic feature of non-trivial topology is found just below the Fermi level (E_F) at the Γ point, where an inversion takes place between two bands made of S p_{xy} and W d_{zy}/d_{zx} orbitals [5, 19, 22]. The upper electron-like band of the pair crosses the Fermi level along the N-Γ-N_1 direction (see Fig. S1 in the SM [46] for the high-symmetry points in the BZ of 2M-WS$_2$). Another hole-like band of predominantly W d_{zy}/d_{zx} characters is also present at the Fermi level. This band has a camel shape with the two humps crossing the Fermi level along the N_1-Y and Y-M directions, respectively. As has been found in Refs. 5 and 20, these multiple crossings at the Fermi level give rise to a complex FS structure with eight sheets. The density of states (DOS) along with the orbital resolved contributions is also shown in the right panel of Fig. 3(a). The S p_{xy} orbitals give almost half of the total DOS, while approximately 20% comes from the W d_{zy}/d_{zx} orbitals. In accordance with previous studies [19, 27], the inclusion of spin-orbit coupling (SOC) is found to have only a minor effect. In particular, there is a small (33 meV) increase in the size of the gap formed between the valence and conduction bands just below the Fermi level at the Γ point (see Fig. S2(a) in the SM [46]). Since the DOS remains largely unaffected over a wide energy window, the effect of SOC is not taken into consideration when we explore the effect of doping.

We further examine how substitutional doping at the W sites affects the electronic properties of 2M-WS$_2$. Fig. 3(b, d-e) shows the electronic band structure and DOS at 50% doping with Mo, Nb, and Ta. Results at other doping levels with the VCA method are shown in Figs. S3(a), S4(a), and S5(a) in the SM [46]. For Mo doping, the Γ-centered S p_{xy} electron pocket moves up in energy relative to the Fermi level. A similar behavior is also observed at the Y point, where another pocket made of S p_{xy} orbitals extends towards the conduction band and crosses the Fermi level. In 2M-MoS$_2$, the tip of this hole-like band lies just above the Fermi level, and merges with the Mo $d_{x^2-y^2}$ electron pocket forming a Dirac point crossing, as shown in Fig. 3(c). With such electronic rearrangements, there are also noticeable changes in the DOS profile. For instance, the peak present in the DOS at the Fermi level in 2M-WS$_2$ is shifted upwards, leading to a 20% decrease in the DOS at E_F in 2M-MoS$_2$.

When doping with the nearby transition metals in the periodic table Nb and Ta, the bands of predominant W d_{zy}/d_{zx} characters in the undoped system (blue dots in Fig. 3(a)) are pushed up and the band inversion at the Γ-point is removed. Since the mixed compounds are p-doped, the Fermi level is positioned deeper into the valance band and the DOS at the Fermi level (N_{F}) increases by approximately 20%. Compared to 2M-WS$_2$, the S p_{xy} states do not provide anymore the dominant contribution to the DOS at E_F.

The effect of doping at the S sites with Se is shown in Fig. 3(f-g) and Fig. S6(a) in the SM [46]. With increasing Se concentration, the Γ-centered electron pocket of chalcogen p_{xy} character widens and elongates, while the hole pockets near the Y point shrink. These changes in the band structure give rise to a monotonic decrease in the DOS at the Fermi level. In 2M-WSe$_2$, N_{F} is about two times lower than in 2M-WS$_2$.

To investigate intermediate doping levels we used the VCA method. Several studies have pointed out that this approach has certain limitations in describing the electronic properties [47, 48]. As shown in Fig. S7(a-c) in the SM [46], we find good agreement between the VCA and subsitutional doping results when doping at the W sites with Mo, Nb and Ta. While the agreement slightly deteriorates for Se doping at the S sites as shown in Fig. S8(a) and (c) in the SM [46], the main features in the vicinity of the Fermi level are well captured. The small discrepancies observed at the Γ and Y points are expected because the broken structural symmetry and local distortions that take place in the calculations with substitutional doping are not captured by the VCA method. Importantly, N_{F} is found to be comparable between the two sets of calculations. This provides additional support for employing the VCA method for concentration levels that would otherwise require calculations with large supercells with the substitutional approach.

PHONON DISPERSION AND ELECTRON-PHONON PROPERTIES

Figure. 4(a) shows the calculated phonon dispersion of 2M-WS$_2$ along with the atom-projected phonon density of states (PHDOS), the isotropic Eliashberg spectral function $\alpha^2\mathrm{F}(\omega)$, and the e-ph coupling strength (λ). Two gaps at around 25 meV and 48 meV split the entire spectrum into three parts. The modes in the lower frequency region are primarily related to both in-plane and out-of-plane vibrations of the W atoms, whereas the intermediate and higher frequency modes correspond to the vibrations of the S atoms. This is to be expected considering that the atomic mass of W is more than five times that of S. As for the electronic structure, the effect of the SOC on the phonon dispersion is found to be negligible. These results are in good agreement with previous theoretical calculations [27].

Now we discuss how the phonon spectrum is modified with substitutional doping. The low frequency modes are mainly affected when doping with transition metals Mo, Nb, and Ta at the W sites, while the intermediate and high frequency modes when doping with Se at the S sites. As shown in Fig. 4(b) and Fig. S3(b) in the SM [46], the lower-frequency gap in the phonon spectrum is gradually reduced by increasing the Mo content as the low frequency modes harden. In 2M-MoS$_2$, the gap is completely closed and there is a mixed contribution of similar weight from Mo and S vibrations as can be seen from the mode-resolved PHDOS in Fig. 4(c). On the other hand, the gap widens with Nb and Ta doping since the low frequency modes corresponding to the W vibrations soften (see Fig. 4(d-e)). Finally, for Se doping, there is an overall softening of the phonons in the intermediate and high frequency regions, leading to a decrease in the width of the two gaps as shown in Fig. 4(f-g). Compared to 2M-WS$_2$, the lower gap in the phonon spectrum is absent in 2M-WSe$_2$ and the frequencies corresponding to Se atoms are approximately scaled down by a mass factor $\sqrt{m_{Se}/m_S} = 1.6$ (see Fig. 4(h)).

Additional results with the VCA method at different doping levels are presented in Figs. S3(b), S4(b), S5(b) and S6(b) in the SM [46]. We initially approximated the mass of the virtual atom based on the mixing ratio of the atomic masses of the two species according to expression

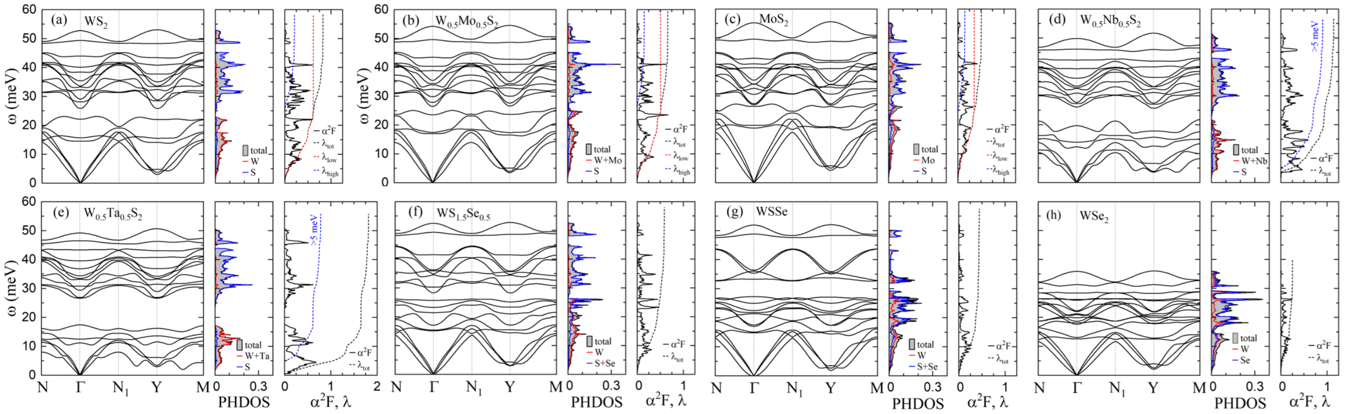

FIG. 4. Phonon dispersion, phonon density of states, Eliashberg spectral function, and e-ph coupling strength of (a) WS_2, (b) $W_{0.5}Mo_{0.5}S_2$, (c) MoS_2, (d) $W_{0.5}Nb_{0.5}S_2$, (e) $W_{0.5}Ta_{0.5}S_2$, (f) $WS_{1.5}Se_{0.5}$, (g) WSSe, and (h) WSe_2 in the 2M phase.

$(1-x)m_{\rm W} + xm_{\rm X}$ (X = Mo, Nb, and Ta) at the W sites and $(1-x)m_{\rm S} + xm_{\rm Se}$ at the S sites, where x is the doping concentration. This approach turned out to work well when doping with transition metals (see Fig. S7(d-f) in the SM [46]), but failed for Se doping where the phonons in the 25-40 meV region were found to be too soft. In this case, we used an alternative approach where the mass of a single atom is scaled, while the other three atoms take the mass of either S or Se according to the doping concentration. The mass of the virtual atom is given by $m_{\rm S} + (4x - n)(m_{\rm Se} - m_{\rm S})$, where $n = 0$ for $0 < x \leq 0.25$, $n = 1$ for $0.25 < x \leq 0.5$, $n = 2$ for $0.5 < x \leq 0.75$, and $n = 3$ for $0.75 < x \leq 1$. As an example for $0.25 < x \leq 0.5$, two atoms have the mass of S, one atom that of Se, and one atom is scaled such that at $x = 0.5$ two atoms will have mass of the Se (i.e., equivalent to replacing two S atoms with Se in the substitutional doping case). As can be seen in Fig. S8(b, d) in the SM [46], we find very good agreement between the phonon spectra calculated with the VCA and substitutional doping when this second mass scaling approach was employed for Se doping. As mentioned earlier, over 50% doping with Nb or Ta leads to dynamical instability as an imaginary mode develops across the whole BZ.

We now move to analyze the e-ph coupling and the superconducting properties. A comparative analysis of the Eliashberg spectral function $\alpha^2{\rm F}(\omega)$ and the atom-projected PHDOS shows that in 2M-WS_2 the low-frequency modes associated with the W vibrations contribute around 75% of the total e-ph coupling strength λ (red dotted lines in Fig. 4(a)) and the remaining 25% comes from the S modes in the intermediate and high frequency regions (blue dotted lines).

Figure 5(a-b) summarizes the dependence of $N_{\rm F}$ and λ as a function of dopant concentration x. Doping with Mo and S leads to a monotonic decrease in λ as both the DOS at the Fermi level and the e-ph coupling due to the low-frequency phonons are reduced with increasing the dopant content. Compared to 2M-WS_2, λ is reduced by approximately 25% in 2M-MoS_2 and almost 60% in 2M-WSe_2. For Nb and Ta doping, λ displays a V-shaped dependence. These two distinct regimes manifest in a sharp drop in λ until the doping level reaches 20% followed by an equally sharp increase to the maximum value at 50% doping. This two-stage behavior is again determined by the combined behavior of the $N_{\rm F}$ and the low-frequency phonons.

We find an overall good level of agreement between the e-ph calculations with the VCA and the substitutional doping approach. For example, at 50% Mo doping and 25% Se doping (Figs. S7(d) and S8(b) in the SM [46]), the two sets of results are almost on top of each other. The discrepancy in the case of Nb and Ta doping is due to the stronger softening of the lowest frequency phonon branch throughout the BZ in the calculations with substitutional doping. As a result, at 50% doping, the e-ph coupling in the region below 5 meV is enhanced by approximately 0.25 and 1.0 for Nb and Ta, respectively. Nevertheless, the two approaches give values that are very close if the contribution from the lowest phonon branch to λ is excluded from the calculations with substitutional doping (see blue and red dotted lines in Fig. 4(d-e)).

To estimate the superconducting $T_{\rm c}$, we solved the isotropic ME equations using a Coulomb pseudopotential $\mu^* = 0.1$. Consistent with previous experimental and theoretical studies [18, 27], we obtain a critical temperature of 8.7 K in 2M-WS_2. Moreover, in line with experimental resistivity measurements, we find that the superconducting $T_{\rm c}$ is reduced with Mo and Se doping [28, 29]. As shown in Fig. 5(c), the variation in $T_{\rm c}$ with doping mirrors the trends observed for the $N_{\rm F}$ and λ. In 2M-MoS_2, the $T_{\rm c}$ drops to 2.5 K, while in 2M-WSe_2, the superconductivity is completely suppressed. On the other hand, the critical temperature of 2M-WS_2 could be enhanced to 10.8 K and 11.6 K at 50% doping with Nb or Ta, respectively. For completeness, we also doped Te at

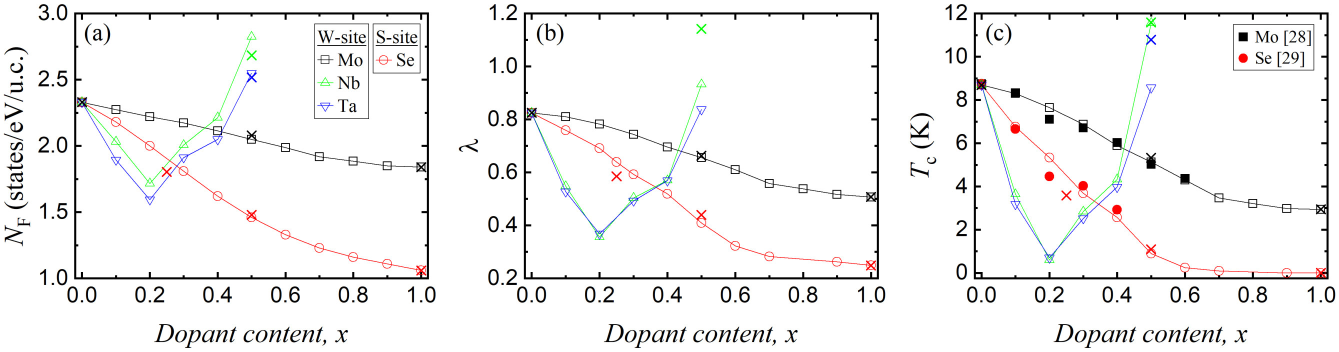

FIG. 5. Variation of (a) DOS at the Fermi level N_F, (b) e-ph coupling strength λ, and (c) T_c as a function of dopant content x. Calculated results with substitutional doping and the VCA method are shown with cross and open symbols. In (c), experimental data for Mo [28] and Se [29] doping are shown with filled symbols.

S sites and transition metals Tc and Re at W sites. We found that the system remains dynamically stable within the full doping range in the Te case, while it becomes dynamical unstable above 35% doping with Re or Tc. No increase in the critical temperature was found for any of these three dopants.

CONCLUSIONS

We studied the superconducting properties of doped 2M-WS_2 by employing the isotropic Migdal-Eliashberg theory. The monotonous decrease in the superconducting critical temperature observed experimentally for Mo and Se doping is remarkably well reproduced by our first-principles calculations. In addition, we find an intriguing V-shaped variation of the superconducting transition temperature with Nb and Ta content and predict that the T_c may be enhanced by a factor of about 1.5 at 50% doping. We also show that the change in the critical temperature with doping can be explained by the dependence of the density of states at the Fermi level and the electron-phonon coupling of the low frequency phonons. We hope that our findings will motivate future experimental work on tuning the superconducting properties of 2M-WS_2 with Nb and Ta doping.

ACKNOWLEDGMENTS

We acknowledge support from the National Science Foundation (Award No. 2035518). This work used the Extreme Science and Engineering Discovery Environment (XSEDE) [49] which is supported by National Science Foundation grant number ACI-1548562. Specifically, this work used Comet/Expanse at the San Diego Supercomputer Center through allocation TG–DMR180071.

---

[*] rmargine@binghamton.edu

[1] B. Radisavljevic, A. Radenovic, J. Brivio, V. Giacometti, and A. Kis, “Single-layer MoS_2 transistors”, Nat. Nanotechnol., **6**, 147-150 (2011).

[2] Q. H. Wang, K. Kalantar-Zadeh, A. Kis, J. N. Coleman, and M. S. Strano, “Electronics and optoelectronics of two-dimensional transition metal dichalcogenides”, Nat. Nanotechnol. **7**, 699712 (2012).

[3] Y. Li, H. Wang, L. Xie, Y. Liang, G. Hong, and H. Dai, “MoS_2 Nanoparticles Grown on Graphene: An Advanced Catalyst for the Hydrogen Evolution Reaction”, J. Am. Chem. Soc. **133**, 72967299 (2011).

[4] Y. Qi, P. G. Naumov, M. N. Ali, C. R. Rajamathi, O. Barkalov, Y. Sun, C. Shekhar, S.-C. Wu, V. Süß, M. Schmidt, E. Pippel, P. Werner, R. Hillebrand, T. Förster, E. Kampertt, W. Schnelle, S. Parkin, R. J. Cava, C. Felser, B. Yan, and S. A. Medvedev, “Superconductivity in Weyl semimetal candidate $MoTe_2$”, Nat. Commun. **7**, 11038 (2016).

[5] Y. Fang, J. Pan, D. Dongqin, D. Wang, H. T. Hirose, T. Terashima, S. Uji, Y. Yuan, W. Li, Z. Tian, J. Xue, Y. Ma, W. Zhao, Q. Xue, G. Mu, H. Zhang, and F. Huang, “Discovery of Superconductivity in 2M WS_2 with Possible Topological Surface States”, Adv. Mater. **31**, 1901942 (2019).

[6] D. L. Greenaway and R. Nitsche,“Preparation and optical properties of Group IV-VI_2 chalcogenides having the CdI_2 structure”, J. Phys. Chem. Solids **26**, 1445 (1965).

[7] Q. Zhao, Y. Guo, K. Si, Z. Ren, J. Bai, and X. Xu, “Elastic, electronic, and dielectric properties of bulk and monolayer ZrS_2, $ZrSe_2$, HfS_2, $HfSe_2$ from van der Waals density-functional theory”, Phys. Status Solidi B **254**, 1700033 (2017).

[8] S. Kim, A. Konar, W.S. Hwang, J.H. Lee, J. Lee, J. Yang, C. Jung, H. Kim, J.B. Yoo, J.Y. Choi, and Y.W. Jin, “High-mobility and low-power thin-film transistors based on multilayer MoS_2 crystals”, Nat. Commun., **3**, 1011 (2012).

[9] M.W. Iqbal, M.Z. Iqbal, M.F. Khan, M.A. Shehzad, Y. Seo, J.H. Park, C. Hwang, and J. Eom, “High-mobility and air-stable single-layer WS_2 field-effect transistors sandwiched between chemical vapor deposition-

grown hexagonal BN films", Sci. Rep. **5**, 10699 (2015).

[10] Y. K. Luo, J. Xu, T. Zhu, G. Wu, E. J. McCormick, W. Zhan, M. R. Neupane, and R. K. Kawakami, "Opto-Valleytronic Spin Injection in Monolayer MoS_2/Few-Layer Graphene Hybrid Spin Valves", Nano Lett., **17**, 3877-3883 (2017).

[11] J. R. Schaibley, H. Yu, G. Clark, Pas. Rivera, Ja. S. Ross, K. L. Seyler, W. Yao, and X. Xu, "Valleytronics in 2D materials", Nat. Rev. Mater., **1**, 16055 (2016).

[12] M. N. Ali, J. Xiong, S. Flynn, J. Tao, Q. D. Gibson, L. M. Schoop, T. Liang, N. Haldolaarachchige, M. Hirschberger, N. P. Ong, and R. J. Cava, "Large, non-saturating magnetoresistance in WTe_2", Nature **514**, 205 (2014).

[13] H. Paudyal, S. Poncé, F. Giustino, and E. R. Margine, "Superconducting properties of $MoTe_2$ from *ab initio* anisotropic Migdal-Eliashberg theory", Phys. Rev. B **101**, 214515 (2020).

[14] I. Guillamón, H. Suderow, S. Vieira, L. Cario, and P. Diener, and P. Rodière, "Superconducting Density of States and Vortex Cores of 2H-NbS_2", Phys. Rev. Lett. **101**, 166407 (2008).

[15] F. Weber, S. Rosenkranz, J.-P. Castellan, R. Osborn, R. Hott, R. Heid, K.-P. Bohnen, T. Egami, A. H. Said, and D. Reznik,"Extended Phonon Collapse and the Origin of the Charge-Density Wave in 2H-$NbSe_2$", Phys. Rev. Lett. **107**, 107403 (2011).

[16] C. Heil, S. Poncé, H. Lambert, M. Schlipf, E. R. Margine, and F. Giustino, "Origin of Superconductivity and Latent Charge Density Wave in NbS_2", Phys. Rev. Lett. **119**, 087003 (2017).

[17] R. Bianco, I. Errea, L. Monacelli, M. Calandra, and F. Mauri, "Quantum Enhancement of Charge Density Wave in NbS_2 in the Two-Dimensional Limit", Nano Lett. **19**, 3098-3103 (2020).

[18] Y. Q. Fang, D. Wang, W. Zhao and F. Q. Huang, "Large magnetoresistance in the monoclinic 2M-WSe_2", Europhys. Lett. **131**, 10005 (2020).

[19] N. Joseph, and A. Narayan, "Topological Properties of Bulk and Bilayer 2M-WS_2: A First-Principles Study", J. Phys.: Condens. Matter **33**, 465001 (2021).

[20] Y. W. Li, H. J. Zheng, Y. Q. Fang, D. Q. Zhang, Y. J. Chen, C. Chen, A. J. Liang, W. J. Shi, D. Pei, L. X. Xu, S. Liu, J. Pan, D. H. Lu, M. Hashimoto, A. Barinov, S. W. Jung, C. Cacho, M. X. Wang, Y. He, L. Fu, H. J. Zhang, F. Q. Huang, L. X. Yang, Z. K. Liu, and Y. L. Chen, "Observation of topological superconductivity in a stoichiometric transition metal dichalcogenide 2M-WS_2", Nature Commun., **12**, 2874 (2021).

[21] Y. Fang, Q. Dong, J. Pan, H. Liu, P. Liu, Y. Sun, Q. Li, W. Zhao, B. Liu, and F. Huang, "Observation of superconductivity in pressurized 2M WSe_2 crystals", J. Mater. Chem. C **7**, 8551-8555 (2019).

[22] Z. Guguchia, D. J. Gawryluk, M. Brzezinska, S. S. Tsirkin, R. Khasanov, E. Pomjakushina, F. O. von Rohr, J. A. T. Verezhak, M. Z. Hasan, T. Neupert, H. Luetkens, and A. Amato, "Nodeless superconductivity and its evolution with pressure in the layered dirac semimetal 2M-WS_2", npj Quantum Mater. **4**, 1-8 (2019).

[23] L. S. Wang, Y. Q. Fang, Y. Y. Huang, E. J. Cheng, J. M. Ni, B. L. Pan, Y. Xu, F. Q. Huang, and S. Y. Li, "Nodeless superconducting gap in the topological superconductor candidate $2MWS_2$", Phys. Rev. B **102**, 024523 (2020).

[24] Y. Yuan, J. Pan, X. Wang, Y. Fang, C. Song, L. Wang, K. He, X. Ma, H. Zhang, F. Huang, W. Li, and Q. Xue, "Evidence of anisotropic Majorana bound states in 2M-WS_2", Nat. Phys. **15**, 1046-1051 (2019).

[25] S. Poncé, E. R. Margine, C. Verdi, and F. Giustino, "EPW: Electron-phonon coupling, transport and superconducting properties using maximally localized Wannier functions", Comput. Phys. Commun. **209**, 116 (2016).

[26] E. R. Margine and F. Giustino, "Anisotropic Migdal-Eliashberg theory using Wannier functions", Phys. Rev. B **87**, 024505 (2013).

[27] C. Lian, C. Si, and W. Duan, "Anisotropic full-Gap superconductivity in 2M-WS_2 topological metal with intrinsic proximity effect", Nano Lett. **21**, 709-715 (2020).

[28] C. Zhao, X. Che, Z. Zhang, and F. Huang, "P-type doping in 2M-WS_2 for a complete phase diagram", Dalton Trans. **50**, 3862-3866 (2021).

[29] C. Zhao, X. Che, Y. Fang, X. Liu, and F. Huang, "Suppression of the superconducting transition temperature in Se-doping 2M-WS_2", J. Phys. Chem. Solids **149**, 109789 (2021).

[30] P. B. Allen and B. Mitrović, "Theory of superconducting T_c", Solid State Phys. **37**, 1 (1982).

[31] P. Giannozzi, O. Andreussi, T. Brumme, O. Bunau, M. B. Nardelli, M. Calandra, R. Car, C. Cavazzoni, D. Ceresoli, M. Cococcioni *et al.*, "Advanced capabilities for materials modelling with Quantum ESPRESSO", J. Phys.: Condens. Matter **29**, 465901 (2017).

[32] D. R. Hamann, "Optimized norm-conserving vanderbilt pseudopotentials", Phys. Rev. B **88**, 085117 (2013).

[33] M. Schlipf and F. Gygi, "Optimization algorithm for the generation of ONCV pseudopotentials", Comput. Phys. Commun. **196**, 36 (2015).

[34] J. P. Perdew, K. Burke, and M. Ernzerhof, "Generalized gradient approximation made simple", Phys. Rev. Lett. **77**, 3865 (1996).

[35] J. Klimeš, D. R. Bowler, and A. Michaelides, "Van der Waals density functionals applied to solids", Phys. Rev. B **83**, 195131 (2011).

[36] T. Thonhauser, V. R. Cooper, S. Li, A. Puzder, P. Hyldgaard, and D. C. Langreth, "Van der Waals density functional: Self-consistent potential and the nature of the van der Waals bond", Phys. Rev. B **76**, 125112 (2007).

[37] T. Thonhauser, S. Zuluaga, C. A. Arter, K. Berland, E. Schrder, and P. Hyldgaard, "Spin Signature of Nonlocal Correlation Binding in Metal-Organic Frameworks", Phys. Rev. Lett. **115**, 136402 (2015).

[38] H. J. Monkhorst and J. D. Pack, "Special points for Brillouin-zone integrations", Phys. Rev. B **13**, 5188 (1976).

[39] M. Methfessel and A. T. Paxton, "High-precision sampling for Brillouin-zone integration in metals", Phys. Rev. B **40**, 3616 (1989).

[40] S. Hajinazar, A. Thorn, E. D. Sandoval, S. Kharabadze and A. N. Kolmogorov, "MAISE: Construction of neural network interatomic models and evolutionary structure optimization", Comput. Phys. Commun. **259**, 107679 (2020).

[41] S. Baroni, S. de Gironcoli, A. Dal Corso, and P. Giannozzi, "Phonons and related properties of extended systems from density-functional perturbation theory", Rev. Mod. Phys. **73**, 515 (2001).

[42] F. Giustino, M. L. Cohen, and S. G. Louie, "Electron-

phonon interaction using Wannier functions", Phys. Rev. B **76**, 165108 (2007).

[43] N. Marzari, A. A. Mostofi, J. R. Yates, I. Souza, and D. Vanderbilt, "Maximally localized Wannier functions: Theory and applications", Rev. Mod. Phys. **84**, 1419 (2012).

[44] G. Pizzi, V. Vitale, R. Arita, S. Bluegel, F. Freimuth, G. Géranton, M. Gibertini, D. Gresch, C. Johnson, T. Koretsune *et al.*, "Wannier90 as a community code: new features and applications", J. Phys.: Condens. Matter **32(16)**, 165902 (2019).

[45] G. P. Kafle, C. Heil, H. Paudyal, and E. R. Margine, "Electronic, vibrational, and electron-phonon coupling properties in $SnSe_2$ and SnS_2 under pressure", J. Mater. Chem. C, **8**, 16404-16417 (2020).

[46] See Supplemental Material at [url] for Figs. S1-S8.

[47] L. Bellaiche, S-H. Wei, and A. Zunger, "Band gaps of GaPN and GaAsN alloys", Appl. Phys. Lett. **70(26)**, 3558-3560 (1997).

[48] C. Chen, E. G. Wang, Y. M. Gu, D. M. Bylander, and L. Kleinman, "Unexpected band-gap collapse in quaternary alloys at the group-III-nitride/GaAs interface: GaAlAsN", Phys. Rev. B **57(7)**, 3753 (1998).

[49] J. Towns, T. Cockerill, M. Dahan, I. Foster, K. Gaither, A. Grimshaw, V. Hazlewood, S. Lathrop, D. Lifka, G. D. Peterson, R. Roskies, J. R. Scott, N. Wilkins-Diehr, "XSEDE: Accelerating scientific discovery", Comput. Sci. & Eng. **16**, 62-74 (2014).